

I-INR: Iterative Implicit Neural Representations

Ali Haider^{1*}, Muhammad Salman Ali^{1*}, Maryam Qamar¹,
Tahir Khalil¹, Soo Ye Kim², Jihyong Oh³, Enzo Tartaglione⁴, Sung-Ho Bae^{1†}

¹ Kyung Hee University, Republic of Korea

² Adobe Research

³ Chung-Ang University, Republic of Korea

⁴LTCI, Télécom Paris, Institut Polytechnique de Paris, France

{alishaider, salmanali, maryamqamar, tahirkhalil26}@khu.ac.kr,

sooyek@adobe.com, jihyongoh@cau.ac.kr,

enzo.tartaglione@telecom-paris.fr, shbae@khu.ac.kr

Abstract

Implicit Neural Representations (INRs) have revolutionized signal processing and computer vision by modeling signals as continuous, differentiable functions parameterized by neural networks. However, their inherent formulation as a regression problem makes them prone to regression to the mean, limiting their ability to capture fine details, retain high-frequency information, and handle noise effectively. To address these challenges, we propose Iterative Implicit Neural Representations (I-INRs) a novel plug-and-play framework that enhances signal reconstruction through an iterative refinement process. I-INRs effectively recover high-frequency details, improve robustness to noise, and achieve superior reconstruction quality. Our framework seamlessly integrates with existing INR architectures, delivering substantial performance gains across various tasks. Extensive experiments show that I-INRs outperform baseline methods, including WIRE, SIREN, and Gauss, in diverse computer vision applications such as image restoration, image denoising, and object occupancy prediction.

1. Introduction

Implicit Neural Representations (INRs) have emerged as a transformative approach in signal representation, shifting from traditional discrete grid-based methods to continuous coordinate-based models [39]. By leveraging neural networks, typically multi-layer perceptrons (MLPs), INRs map spatial or temporal coordinates directly to signal attributes such as pixel intensity, colour, or 3D occupancy. This continuous representation inherently offers resolution indepen-

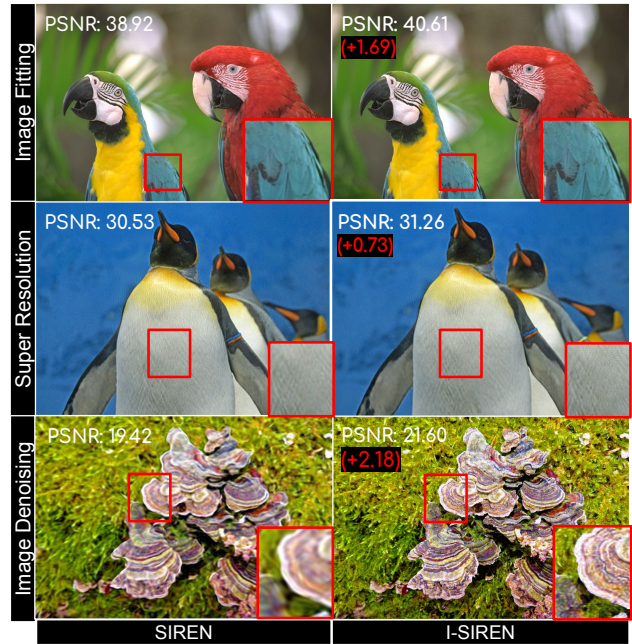


Figure 1. Effectiveness of the proposed methods across multiple tasks, including image fitting, Super Resolution (2× scale), and denoising, compared to the baseline representative INR method (SIREN [39]). Our novel Iterative-INR method (I-SIREN) consistently improves detail preservation, fidelity, and high-frequency reconstruction across all tasks, outperforming the baseline.

dence, compact encoding, and seamless interpolation, making INRs highly versatile across a wide range of domains including computer vision [5, 18, 24, 35, 39], and beyond [31, 37, 42, 49]. Initially introduced for tasks like 3D shape reconstruction [24, 26, 41] and novel view synthesis [17], INRs have since been applied to diverse applications including image fitting [23], super-resolution [9, 34], and solving

*Equal Contribution † Corresponding Author

inverse problems [3, 5, 44].

Despite advancements, INRs continue to face substantial challenges in capturing high-frequency details, maintaining robustness against noise, and handling incomplete data [36]. Typically optimized with L1 or L2 loss [39], INRs exhibit a bias toward low-frequency components due to the regression to the mean effect, leading to the loss of high-frequency details and reduced noise robustness [9]. Recent works have tried to solve this problem through positional encoding techniques [43] or by incorporating new activation functions [23, 36, 39]. Positional encoding techniques [43] incorporate various orthogonal Fourier [11], while periodic activations, such as sine functions, allow MLPs to better model high-frequency signals compared to conventional ReLU activations [39]. However, these methods are often based on the assumption of clean, noise-free data, which limits their applicability in real-world scenarios where noise and missing information are prevalent [36]. Advanced activation functions like complex Gabor wavelets have been proposed to enhance noise robustness [36], but these approaches still fall short when handling the complexities of challenging, real-world datasets. Despite these efforts, there remains significant potential for further improving high-frequency detail preservation, representational accuracy, and reconstruction quality in INRs.

To address these limitations, drawing inspiration from iterative models [9, 15, 33], we introduce *Iterative Implicit Neural Representations (I-INRs)*, a plug-and-play framework that integrates seamlessly with existing implicit architectures. Unlike traditional single-shot INRs, I-INRs reconstruct signals progressively over multiple iterations, refining details, enhancing reconstruction quality, and improving noise robustness as shown in Figure 1. Our experiments demonstrate that I-INRs deliver superior reconstructions with enhanced detail, generalization, and minimal computational overhead, outperforming single-shot methods like WIRE [36], SIREN [39], and Gauss [30] across tasks such as image fitting, Super-Resolution (SR), denoising, and 3D occupancy reconstruction.

Our main contributions are.

- We present **Iterative Implicit Neural Representations**, called **I-INRs**, a novel framework that reconstructs signals *iteratively*, effectively capturing high-frequency details, enhancing robustness to noise, and improving generalization.
- I-INRs are designed as a plug-and-play framework, compatible with existing implicit architectures, enabling seamless integration and adoption in various applications.
- We validate the effectiveness of I-INRs through extensive experiments across multiple tasks, demonstrating superior performance over traditional single-shot INRs in terms of detail reconstruction and robustness.

2. Related Work

INRs [39] map coordinates to signal values using neural networks, eliminating the need for discretization and thus offering flexibility in applications such as image, video processing [4, 5, 7, 14, 46], and 3D rendering [13, 24, 32]. However, INRs often suffer from spectral bias [29, 43], struggling to capture high-fidelity details of complex signals. This limitation affects applications requiring fine-grained detail, such as image SR, 3D reconstruction, and scene modeling. To address this challenge, various approaches have been proposed, including spatial encoding with frequency-based representations, polynomial decomposition [28, 38], and high-pass filtering [11], all of which emphasize high-frequency components. Beyond encoding techniques, the choice of activation functions also plays a crucial role in mitigating spectral bias. Standard activations like ReLU fail to capture high-frequency components due to their limited representational capacity [39]. To overcome this, alternative activation functions, such as sinusoidal [39] and Gaussian [30] activations, have been proposed. Additionally, approaches like WIRE [36] and FINER [23] introduce advanced activation strategies to enhance spectral bias tuning, with WIRE [36] leveraging Gabor wavelets and FINER [23] utilizing variable-periodic functions. INCODE [19] uses a task-specific pre-trained model that dynamically adjusts key parameters of activation function to enhance reconstruction performance. DINER [47] utilizes a hash map to unevenly map input coordinates onto a feature vector, optimizing the spatial frequency distribution and enabling faster, more precise reconstructions. While advanced encoding strategies and activation functions help mitigate spectral bias, they may not fully address the challenges of wide-bandwidth signals and large-scale data [21, 35]. To scale INRs for wide-bandwidth signals, hierarchical and multi-scale designs like Progressive Implicit Networks (PINs) [21] and MINER [35] leverage hierarchical encoding and Laplacian pyramids, enabling efficient multi-scale detail capture while reducing computational overhead.

In contrast with single shot models, iterative models, such as diffusion models [9, 15, 33], generate high-quality samples by inverting known degradation processes. These models are widely used for diverse image processing tasks, including image restoration and translation [6, 8, 9, 16, 33, 34]. Furthermore, diffusion models have also been applied to 3D reconstruction tasks from text prompts or 2D images [22, 27]. Inspired by the strong detail reconstruction capabilities of iterative models, we propose a novel INR framework that reconstructs signals implicitly over multiple steps. Our method is a flexible, plug-and-play approach that can be integrated into any existing INR framework. However, for the scope of this paper, we specifically focus on WIRE [36], Gauss [30], and SIREN [39].

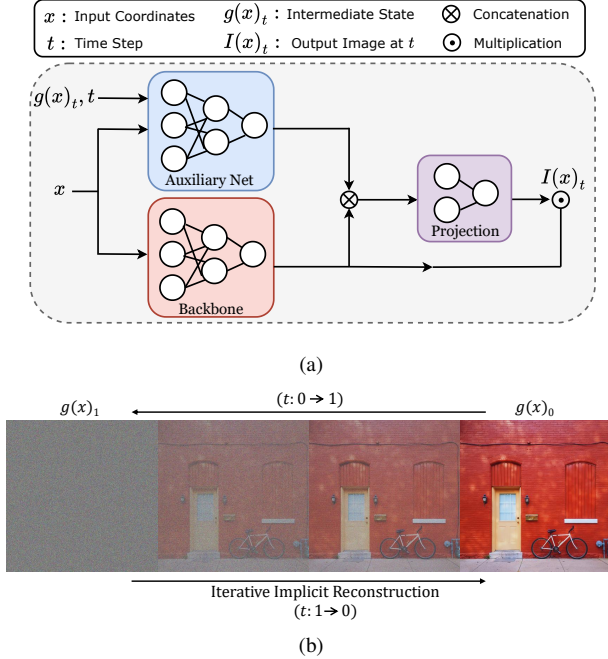


Figure 2. (a) The proposed architecture of the I-INR model. The framework consists of a Base INR, which can be any baseline architecture, denoted as Backbone, such as SIREN [39], WIRE [36], or Gauss [30]. Additionally, an Auxiliary Network incorporates feedback to refine representations, while a projection layer integrates features. The final output is obtained by combining the outputs of the Base INR and the projection layer, enhancing expressivity and reconstruction quality. (b) Iterative reconstruction processes of the proposed I-INR framework.

3. Proposed Method

In this section, we first provide an overview of INRs, followed by a detailed explanation of our proposed method, I-INR.

3.1. Preliminary: Standard INR

Let $g : X \subseteq \mathbb{R}^p \rightarrow Y \subseteq \mathbb{R}^q$ be a target function mapping p -dimensional inputs (such as pixel positions in a 2D image or volumetric domains in 3D scenes) to q -dimensional outputs (such as color or density values), so that $y = g(x)$ for $x \in X$. An INR [39] is a learnable neural function $f_\theta : X \rightarrow Y$, parameterized by θ , aiming to approximate $\mathcal{I}(x)$ across X [36]. The objective is to find θ such that:

$$f_\theta(x) \approx \mathcal{I}(x), \quad (1)$$

where $\mathcal{I}(x)$ represents an image function with pixel coordinates as x . A typical INR is trained by reducing the signal

error in some L_p metric,

$$\min_{\theta} \mathbb{E}_{x, \mathcal{I}(x)} \|f_\theta(x) - \mathcal{I}(x)\|_p \approx \min_{\theta} \sum_i \|f_\theta(x^i) - \mathcal{I}(x^i)\|_p, \quad (2)$$

where $p = 2$, the optimal minimum mean squared error (MMSE) solution is the conditional expectation as in Eq. (3)

$$\mathbb{E}[\mathcal{I}(x) | x] = \int \mathcal{I}(x) p(\mathcal{I}(x) | x) d\mathcal{I}(x). \quad (3)$$

This expectation leads to a signal that represents the average of all plausible reconstructions, often resulting in the loss of fine details. Such an approach limits the ability to capture high-frequency components and makes the reconstruction susceptible to noise. To overcome these limitations, we propose an iterative reconstruction approach that refines the signal progressively over multiple steps as formulated in Section 3.2. This iterative method enables a more precise reconstruction, enhancing frequency details and improving robustness to noise.

3.2. Iterative Implicit Neural Representations: I-INRs

Our proposed method reconstructs the signal in multiple steps, improving the reconstruction quality at each step. The function $g(x)_t$ at any time step t can be defined as:

$$g(x)_t = \mathcal{I}(x)(1-t) + \mathcal{Z}t, \quad t \in [0, 1], \quad (4)$$

where \mathcal{Z} is sampled from a known distribution with the same dimensions as $\mathcal{I}(x)$. The process in Eq. (4) linearly interpolates between $\mathcal{I}(x)$ and \mathcal{Z} using the time step t . At $t = 0$, $g(x)_0$ equates to $\mathcal{I}(x)$, while at $t = 1$, $g(x)_1$ is \mathcal{Z} . Thus, $g(x)_t$ smoothly transitions from $\mathcal{I}(x)$ to \mathcal{Z} as t moves from 0 to 1, providing a continuous interpolation between the two known states as shown in Figure 2b.

During the iterative restoration process, we start from \mathcal{Z} at $t = 1$ and move toward the final reconstruction gradually. Let, $g(x)_s$ and $g(x)_t$ represent some intermediate states such that $s \leq t$. Then the conditional mean is given by:

$$\mathbb{E}(g(x)_s | g(x)_t) = \left(1 - \frac{s}{t}\right) \mathbb{E}(g(x)_0 | g(x)_t) + \frac{s}{t} g(x)_t. \quad (5)$$

When, $s = t - \delta$, then the estimated state $\hat{g}(x)_{t-\delta}$ is given by the Eq. 6 as:

$$\begin{aligned} \hat{g}(x)_{t-\delta} &= \mathbb{E}(g(x)_{t-\delta} | g(x)_t) \\ &= \frac{\delta}{t} \mathbb{E}(g(x)_0 | \hat{g}(x)_t) + \left(1 - \frac{\delta}{t}\right) \hat{g}(x)_t. \end{aligned} \quad (6)$$

Following Eq. (6), the reconstruction process begins at $g(x)_1 = \mathcal{Z}$, with $t = 1$. The final reconstruction is approached iteratively, taking steps of size δ , by estimating the signal at each intermediate step.

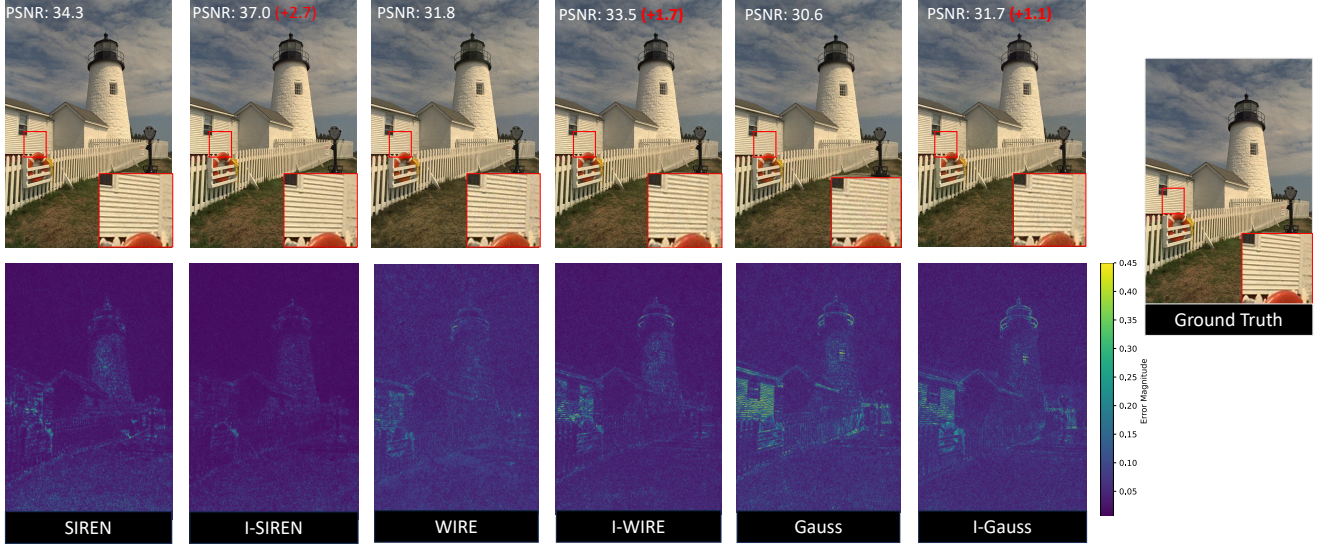


Figure 3. Image fitting results for different non-linearities and their iterative extensions (prefix "I"). Each column presents the reconstructed image (top) and residual map (bottom), highlighting reconstruction quality. PSNR values are reported, with iterative improvements in red. The rightmost column shows the ground truth.

Furthermore, taking the limit $\delta \rightarrow 0$ in Eq. (6) leads to the following ordinary differential equation (ODE) [40]:

$$\begin{aligned} \frac{dg(x)_t}{dt} &= \lim_{\delta \rightarrow 0} \frac{g(x)_t - g(x)_{t-\delta}}{\delta} \\ &= \frac{g(x)_t - \mathbb{E}[g(x)_0 | g(x)_t]}{t}. \end{aligned} \quad (7)$$

Here, the term $g(x)_t - \mathbb{E}[g(x)_0 | g(x)_t]$ represents the residual error correction in the reconstruction process, where $\frac{1}{t}$ scales the update, allowing larger corrections in the early stages when t is large, while finer adjustments take place as $t \rightarrow 0$, ensuring a smooth and gradual refinement toward $g(x)_0$ effectively preventing over-smoothing.

I-INR Training: Our proposed method aims to generate a progressively refined version of the image at each time step. To achieve this, we estimate a reconstructed version of the signal at each intermediate step t , specifically $\mathbb{E}[g(x)_0 | g(x)_t]$. This is achieved by training our neural function to predict the signal itself at any intermediate time step.

Given $x, I(x) \sim p(x, I(x))$, $\mathcal{Z} \sim p(\mathcal{Z})$, and $t \sim p(t)$, the ideal objective function for this process is defined as:

$$\min_{\theta} \mathbb{E}_{(x, I(x)), \mathcal{Z}} \mathbb{E}_t \|f_{\theta}(g(x)_t, x, t) - I(x)\|_2, \quad (8)$$

where,

$$g(x)_t = \mathcal{I}(x)(1 - t) + \mathcal{Z}t.$$

To follow the regularity requirement mentioned in [9] for the iterative procedure, we add small noise to the intermediate latent state. The model with noise perturbation is given by:

$$\tilde{g}_t(x) = I(x)(1 - t) + \mathcal{Z}t + \epsilon \cdot n \cdot t, \quad (9)$$

where, ϵ denotes a small constant that ensures a controlled amount of noise, and n is a random variable sampled from a standard normal distribution $\mathcal{N}(0, 1)$. Hence, our training objective becomes,

$$\min_{\theta} \mathbb{E}_{(x, I(x)), \mathcal{Z}} \mathbb{E}_t \mathbb{E}_n \|f_{\theta}(\tilde{g}(x)_t, x, t) - I(x)\|_2. \quad (10)$$

The detailed training procedure is provided in Algo. 1.

I-INR Reconstruction: During reconstruction, we start from an initial state \mathcal{Z} and iteratively move towards the final reconstruction over $steps = \frac{1}{\delta}$. Typically, the known function \mathcal{Z} is a simple initial state. Thus, we begin from \mathcal{Z} and iteratively enhance it over time. The iterative implicit reconstruction process is outlined in Algo. 2.

Algorithm 1 I-INRs Model Training f_{θ}

Require: ϵ

$$(x, I(x)) \sim p(x, I(x))$$

$$\mathcal{Z} \sim p(\mathcal{Z})$$

repeat

$$t \sim \mathcal{U}(0, 1)$$

$$n \sim \mathcal{N}(0, 1)$$

$$\tilde{g}_t(x) = I(x)(1 - t) + \mathcal{Z}t + \epsilon \cdot n \cdot t$$

Take a gradient descent step on

$$\nabla_{\theta} \|f_{\theta}(\tilde{g}(x)_t, x, t) - I(x)\|_2$$

until converged

Network Architecture: Figure 2a illustrates the I-INR architecture that integrates an Auxiliary Network and a Back-

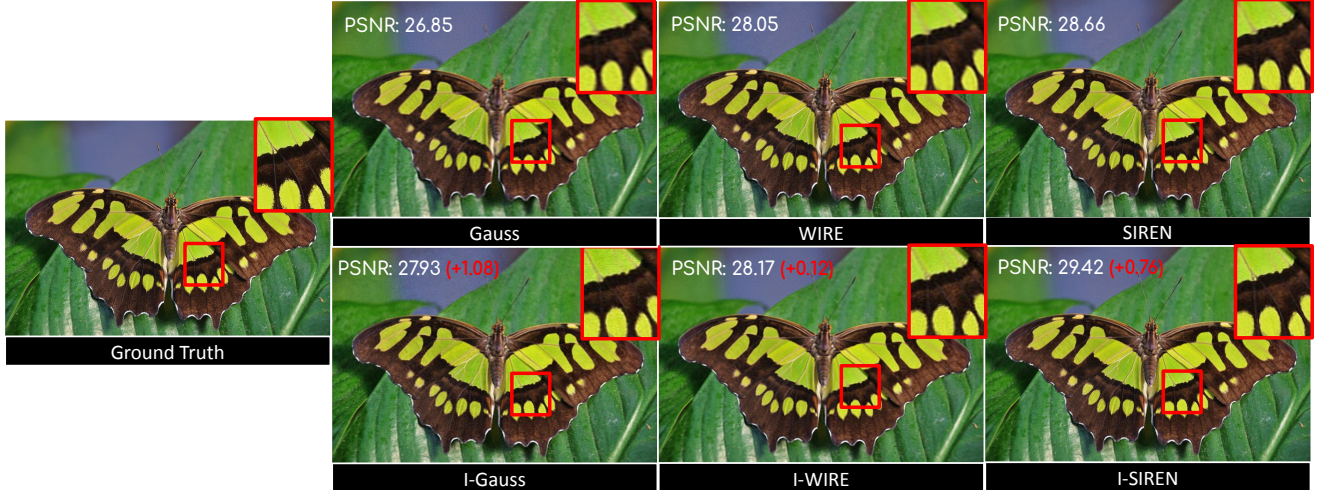


Figure 4. Visual quality comparison of super-resolution results at 2x scale using various methods. The ground truth is compared against baseline INR methods SIREN [39], WIRE [36], Gauss [30], and their iterative counterparts. The iterative approaches consistently achieve sharper reconstructions with fewer artifacts, effectively preserving finer details and high-frequency structures.

Algorithm 2 I-INRs Model Reconstruction

Require: $\mathcal{Z}, f_{\theta}(\cdot, t), \delta, x$
 $\hat{g}(x)_1 = \mathcal{Z}$
for $t \in \{1, 1 - \delta, 1 - 2\delta, \dots, 0\}$ **do** $\triangleright t$ decreases from 1 to 0 in steps of δ
 $\hat{g}(x)_{t-\delta} = \frac{\delta}{t} f_{\theta}(\hat{g}(x)_t, x, t) + (1 - \frac{\delta}{t}) \hat{g}(x)_t$
end for
return $\tilde{g}(x)_0$

bone (such as SIREN) to compute the output $I(x)_t$. The input x is processed independently by both the Auxiliary Network and the Backbone, while the Auxiliary Network also incorporates feedback from the previous step. The output of the Auxiliary Network is concatenated with the features extracted by the Backbone, forming a joint representation. This concatenated feature then passes through a projection layer, which further refines the combined features. The final output is obtained as the dot product of the projection layer and the Backbone.

4. Experiments

To evaluate the effectiveness and robustness of our proposed method, we conduct extensive experiments across diverse tasks and backbones. Our evaluation encompasses regression tasks, such as 2D and 3D signal fitting, as well as generalization and robustness tasks, including image SR and image denoising. To demonstrate its comparative advantage, we benchmark our method against established baseline approaches, including SIREN [39], Gauss [30], and WIRE [36].

Implementation Settings: The proposed I-INR framework is implemented in PyTorch [25] and optimized using the Adam optimizer [10]. For all experiments, the noise parameter ϵ is empirically set to 0.1, and the inference *steps* are fixed to 2 unless stated otherwise. The initial state \mathcal{Z} is sampled from standard normal Gaussian distribution across all experiments. All baseline methods, including SIREN [39], WIRE [36], and Gauss [30], as well as their iterative counterparts, are initialized following the configurations specified in their respective papers. In I-INR, both the Auxiliary Network and the Projection layer employ lightweight MLPs to ensure computational efficiency while preserving expressivity.

Evaluation Metrics: To comprehensively evaluate our proposed method, we conduct extensive experiments using both distortion-based metrics, such as Peak Signal-to-Noise Ratio (PSNR) and Structural Similarity Index Measure (SSIM) [45], as well as perceptual metrics like Learned Perceptual Image Patch Similarity (LPIPS) [48].

4.1. Results

Our results consistently demonstrate that I-INR outperforms existing methods across diverse tasks, including image fitting, SR, and 3D occupancy. It achieves superior reconstruction quality and enhanced robustness compared to baseline approaches (SIREN, WIRE, Gauss).

Image Fitting: For image fitting, we employ SIREN [39], WIRE [36], and Gauss [30], along with their iterative variants. Each network utilizes a three-layer MLP with 300 neurons per layer. In the case of iterative models, this corresponds to the Backbone INR illustrated in Figure 2a. The networks are trained on the full-resolution Kodak dataset

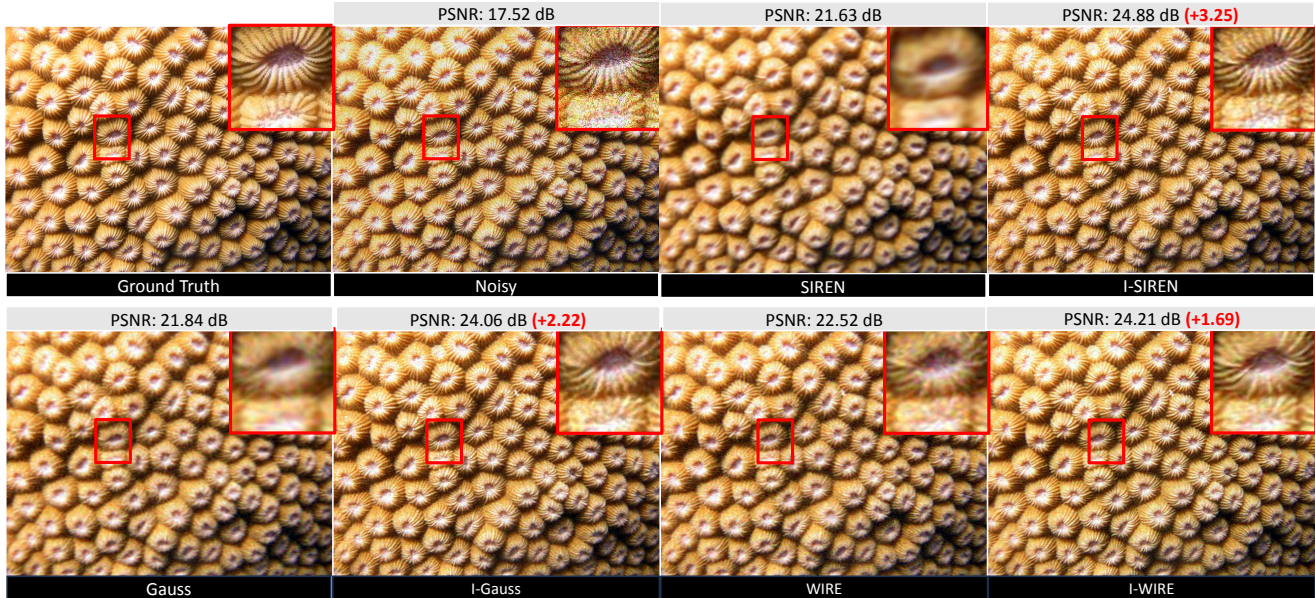


Figure 5. Visual comparison of denoising results using various methods. The ground truth is compared against noisy input, baseline methods SIREN [39], WIRE [36], and Gauss [30], as well as their iterative counterparts. I-INR demonstrates superior artifact reduction and detail preservation compared to their non-iterative counterparts.

Table 1. Image fitting results on the Kodak dataset comparing SIREN [39], WIRE [36], and Gauss [30] with their iterative counterparts. The iterative approach outperforms baseline single-shot architectures by achieving higher reconstruction quality and enhanced fidelity.

	SIREN [39]		WIRE [36]		Gauss [30]	
	PSNR \uparrow	SSIM \uparrow	PSNR \uparrow	SSIM \uparrow	PSNR \uparrow	SSIM \uparrow
Baseline	34.57	0.931	32.15	0.898	31.33	0.880
Ours	37.53	0.961	33.73	0.924	31.93	0.884

(768 \times 512 or 512 \times 768) [20], and the results, averaged across the entire dataset, are presented in Table 1. Our findings demonstrate that the proposed iterative models significantly outperform their one-shot counterparts. Figure 3 provides a qualitative comparison of all networks and their iterative adaptations on the `kodim19` image. The error maps of baseline models exhibit homogeneous noise across the image, with more pronounced errors in high-frequency regions. In contrast, the iterative approaches yield smoother reconstructions with reduced errors throughout the image, including high-frequency areas. This ultimately results in a substantial improvement in fidelity, with PSNR gains of up to 2.7 dB observed for I-SIREN compared to its one-shot equivalent.

Image Super-resolution: We evaluate our I-INR framework against traditional one-shot INRs on SR tasks using 40 images from the DIV2K dataset [1]. The model is trained exclusively on 2 \times SR with a two-layer MLP of 256 neu-

rons per layer. To assess generalization, we evaluate I-INR on both 2 \times and 4 \times SR, despite training only on 2 \times . Table 2 compares its performance with single-shot baselines, demonstrating that our approach consistently enhances fidelity (measured as PSNR) and perceptual quality (measured as LPIPS) across all architectures. Figure 4 visualizes the butterfly image for 2 \times SR (please refer to supplementary material for visualization at 4 \times scale), comparing each baseline with its iterative counterpart. The proposed approach consistently outperforms baseline methods, generating sharper reconstructions with fewer artifacts across all non-linearities. This improvement stems from the iterative process, which progressively refines the reconstruction, enabling more precise recovery of high-frequency details and allowing the model to generalize effectively beyond its training scale.

Table 2. Super-resolution (SR) results for 2 \times and 4 \times evaluations using a model trained exclusively on 2 \times SR. The table compares SIREN [39], WIRE [36], and Gauss [30] with their iterative counterparts. PSNR (higher is better) and LPIPS (lower is better) are reported, with the best result in each column highlighted in **bold**.

Scale Factor	Method	SIREN [39]		WIRE [36]		Gauss [30]	
		PSNR \uparrow	LPIPS \downarrow	PSNR \uparrow	LPIPS \downarrow	PSNR \uparrow	LPIPS \downarrow
2 \times	Baseline	26.77	0.414	26.14	0.457	25.19	0.538
	Ours	27.64	0.367	27.21	0.388	26.82	0.363
4 \times	Baseline	25.03	0.597	24.57	0.6179	23.85	0.673
	Ours	25.53	0.575	25.78	0.496	25.18	0.620

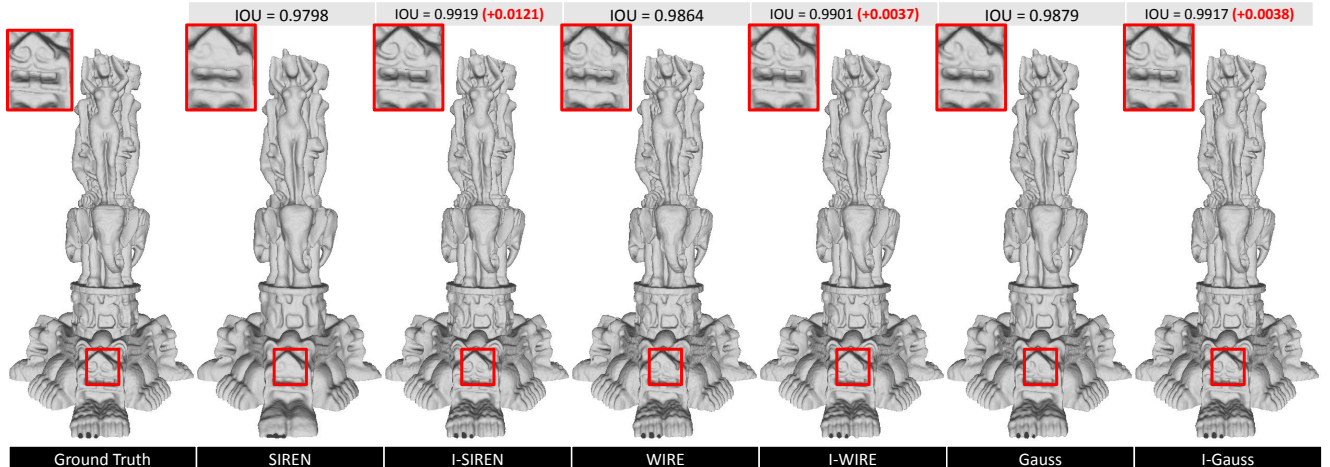


Figure 6. Visualization of 3D occupancy reconstruction results using various methods and their iterative counterparts. The ground truth is compared to baseline models (SIREN [39], WIRE [36], Gauss [30]) and their iterative counterparts. Iterative methods demonstrate superior reconstruction quality, achieving higher Intersection over Union (IOU) scores and capturing finer geometric details.

Table 3. Image denoising results on 40 images sampled from the DIV2K dataset [1], comparing SIREN [39], WIRE [36], and Gauss [30] with their iterative counterparts. The best values in each column are highlighted in **bold**.

	SIREN [39]		WIRE [36]		Gauss [30]	
	PSNR \uparrow	LPIPS \downarrow	PSNR \uparrow	LPIPS \downarrow	PSNR \uparrow	LPIPS \downarrow
Baseline	23.86	0.604	23.32	0.746	23.10	0.783
Ours	25.59	0.540	24.76	0.490	24.20	0.533

Image Denoising: To assess the robustness of I-INRs in modeling noisy signals, we utilize 40 high-resolution color images from the DIV2K dataset [1] and introduce Poisson-distributed noise to each pixel, with a maximum mean photon count of 30 and a readout noise level of 2, following [36]. The same architecture and training procedure as SR is employed. Table 3 presents quantitative results comparing the denoising performance of SIREN [39], WIRE [36], and Gauss [30] with their iterative counterparts. Across all three methods, the iterative models consistently achieve significant improvements in both PSNR and LPIPS over their single-shot baselines. Figure 5 provides a qualitative comparison of denoising performance for SIREN [39], WIRE [36], and Gauss [30] alongside their iterative versions. The iterative approach significantly enhances reconstruction quality across all architectures, achieving up to +3.25 dB PSNR improvement (for SIREN).

3D Occupancy: The 3D occupancy task aims to reconstruct 3D shapes by modeling the occupancy of points in space. We conduct experiments on the Armadillo, Dragon, and Thai Statue 3D scenes [12], utilizing a two-layer MLP with 256 neurons per layer for both the baseline INRs and their iterative counterparts. Table 4 presents the averaged Intersection over Union (IoU) results, while Figure 6 visu-

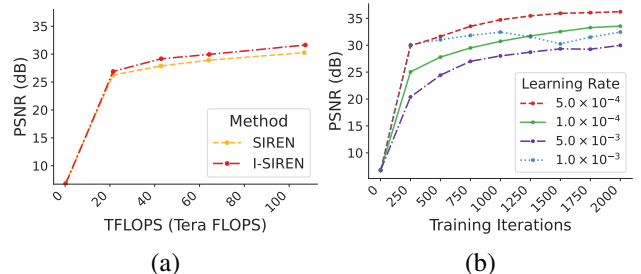


Figure 7. On the Kodak dataset for image fitting: (a) PSNR vs. training FLOPs comparison between SIREN [39] and I-SIREN. (b) PSNR vs. training iterations for I-SIREN with different learning rates.

alizes the reconstructions achieved using different nonlinearities and their iterative variants. Notably, I-INRs outperform their single-shot baselines, generating sharper and more precise reconstructions. The iterative approach enhances detail preservation, particularly in complex regions. For instance, I-SIREN reconstructs significantly finer details at the base of the statue compared to the baseline SIREN, demonstrating its ability to model intricate spatial structures more effectively.

Table 4. Averaged Intersection over Union (IoU) results comparing SIREN [39], WIRE [36], and Gauss [30] with their iterative counterparts on the Armadillo, Dragon, and Thai Statue 3D scenes.

	SIREN[39] \uparrow	WIRE[36] \uparrow	Gauss[30] \uparrow
Baseline	0.9840	0.9917	0.9855
Ours	0.9934	0.9950	0.9967

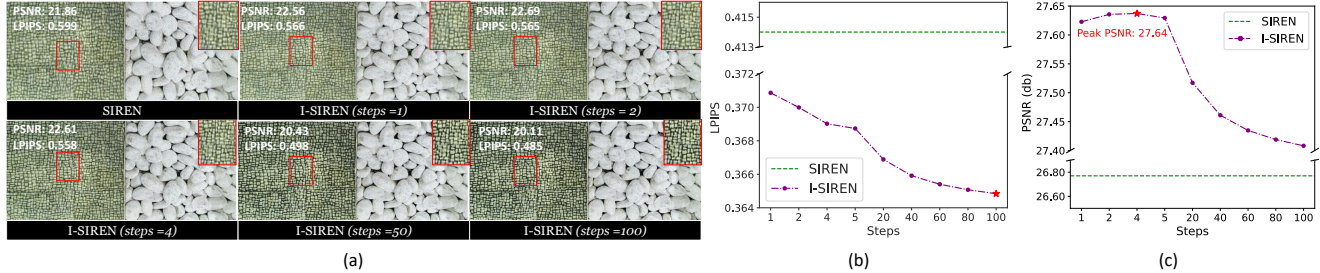


Figure 8. Analysis of I-SIREN’s performance for super-resolution at $2\times$ resolution across different iteration *steps*. (a) I-SIREN achieves peak PSNR at *steps* = 4, where further increasing time steps enhances perceptual quality but reduces fidelity due to the fidelity-perception tradeoff. (b) Increasing the number of steps consistently improves perceptual quality. (c) PSNR reaches its highest performance at *steps* = 4, and while additional iterations slightly reduce PSNR, it remains superior to the baseline.

4.2. Ablation Studies

Initial State: I-INR reconstructs a signal iteratively over multiple steps, starting from an initial state \mathcal{Z} . The choice of this initial state can significantly impact the reconstruction process. To assess its effect, we conduct extensive experiments with different types of initial states. Empirically, \mathcal{Z} sampled from a standard normal Gaussian distribution $\mathcal{N}(0, 1)$ consistently outperforms all-zeros and all-ones initial states across different non-linearities for the image fitting task. The results, summarized in Table 5, highlight the superiority of noise-based initial states in achieving higher PSNR and SSIM values.

Table 5. Impact of different initial states (\mathcal{Z}) on image fitting performance using the I-INR framework on the Kodak dataset. Noise-based initial states consistently achieve the best results across various non-linearities.

	I-SIREN		I-WIRE		I-Gauss	
	PSNR \uparrow	SSIM \uparrow	PSNR \uparrow	SSIM \uparrow	PSNR \uparrow	SSIM \uparrow
Noise	37.53	0.961	33.73	0.924	31.93	0.884
Ones	37.42	0.961	33.33	0.921	30.96	0.867
Zeros	37.47	0.961	33.39	0.921	31.22	0.882

Training and Inference Complexity: Our proposed I-INR method achieves faster convergence than the non-iterative baseline while maintaining similar training complexity, as shown in Figure 7a. The results are averaged over the Kodak dataset for the image fitting task. Figure 7b further illustrates I-SIREN’s training performance under different learning rates.

While I-SIREN converges faster, this improvement comes at a slightly higher per-iteration computational cost, requiring 107.2 GFLOPS compared to 106.8 GFLOPS for SIREN. Additionally, since I-SIREN reconstructs images iteratively, the total inference cost scales with the number of inference steps. In our experiments, we consistently use *steps* = 2, resulting in a total inference complexity of 214.4 GFLOPS for I-SIREN, compared to 106.8 GFLOPS for SIREN.

Number of Layers: For the image fitting task on the Kodak dataset, we investigate the impact of increasing the number of layers in SIREN and its iterative counterpart, I-SIREN. The results, presented in Table 6, show that while the performance of SIREN saturates beyond a certain depth, specifically at five layers, I-SIREN continues to improve as more layers are added. Notably, a three-layer I-SIREN outperforms a five-layer SIREN, demonstrating the efficiency of the iterative approach.

Table 6. Impact of varying layer depths on the image fitting task using SIREN [39] and I-SIREN on the Kodak dataset. I-SIREN consistently outperforms SIREN [39], with a three-layer I-SIREN achieving higher PSNR than a five-layer SIREN [39].

Layers	I-SIREN		SIREN	
	PSNR	Params (k)	PSNR	Params (k)
3	37.53	274	34.62	273
4	38.71	364	36.60	363
5	39.01	455	36.49	453

Analysis of Reconstruction Steps: We analyze the impact of reconstruction steps on $2\times$ super-resolution using 40 images sampled from the DIV2K dataset, as shown in Figures 8b and 8c. Our findings reveal that the model achieves its highest PSNR at *steps* = 4, with the most significant gain occurring when *steps* increases from 1 to 2. Beyond *steps* = 2, the PSNR begins to plateau. Notably, although PSNR decreases for *steps* > 4, the perceptual quality (measured by LPIPS) continues to improve. This behavior aligns with the Perception-Distortion Tradeoff [2], where introducing additional high-frequency details enhances realism but slightly deviates from the ground-truth, thus lowering distortion-based metrics such as PSNR. Figure 8a presents a visual comparison of SIREN and I-SIREN on an image from DIV2K dataset at various time steps. I-SIREN reconstructions become progressively more vibrant and perceptually appealing as step increases, confirming that additional refinement steps are beneficial for capturing finer textures

and high-frequency components. This trend holds for other reconstruction tasks as well, as detailed in our supplementary material.

5. Conclusion

This work introduces a novel I-INR framework that progressively reconstructs a signal. The proposed method serves as a plug-and-play solution compatible with existing INR methods, significantly enhancing their performance. Through extensive experiments, we demonstrate that I-INR effectively captures high-frequency details, improves noise robustness, and achieves superior reconstruction quality across various tasks and nonlinearities.

References

- [1] Eirikur Agustsson and Radu Timofte. Ntire 2017 challenge on single image super-resolution: Dataset and study. In *Proceedings of the IEEE conference on computer vision and pattern recognition workshops*, pages 126–135, 2017. [6](#), [7](#)
- [2] Yochai Blau and Tomer Michaeli. The perception-distortion tradeoff. In *Proceedings of the IEEE conference on computer vision and pattern recognition*, pages 6228–6237, 2018. [8](#)
- [3] Junghun Cha, Ali Haider, Seoyun Yang, Hoeyeong Jin, Subin Yang, AFM Shahab Uddin, Jaehyoung Kim, Soo Ye Kim, and Sung-Ho Bae. Descanning: From scanned to the original images with a color correction diffusion model. In *Proceedings of the AAAI Conference on Artificial Intelligence*, pages 954–963, 2024. [2](#)
- [4] Hao Chen, Bo He, Hanyu Wang, Yixuan Ren, Ser Nam Lim, and Abhinav Shrivastava. Nerv: Neural representations for videos. In *Advances in Neural Information Processing Systems*, pages 21557–21568. Curran Associates, Inc., 2021. [2](#)
- [5] Yinbo Chen, Sifei Liu, and Xiaolong Wang. Learning continuous image representation with local implicit image function. In *Proceedings of the IEEE/CVF conference on computer vision and pattern recognition*, pages 8628–8638, 2021. [1](#), [2](#)
- [6] Yinbo Chen, Oliver Wang, Richard Zhang, Eli Shechtman, Xiaolong Wang, and Michael Gharbi. Image neural field diffusion models. In *Proceedings of the IEEE/CVF Conference on Computer Vision and Pattern Recognition*, pages 8007–8017, 2024. [2](#)
- [7] Zeyuan Chen, Yinbo Chen, Jingwen Liu, Xingqian Xu, Vidit Goel, Zhangyang Wang, Humphrey Shi, and Xiaolong Wang. Videoinr: Learning video implicit neural representation for continuous space-time super-resolution. In *Proceedings of the IEEE/CVF Conference on Computer Vision and Pattern Recognition (CVPR)*, pages 2047–2057, 2022. [2](#)
- [8] Jiayue Chu, Chenhe Du, Xiyue Lin, Xiaoqun Zhang, Lihui Wang, Yuyao Zhang, and Hongjiang Wei. Highly accelerated mri via implicit neural representation guided posterior sampling of diffusion models. *Medical Image Analysis*, 100: 103398, 2025. [2](#)
- [9] Mauricio Delbracio and Peyman Milanfar. Inversion by direct iteration: An alternative to denoising diffusion for image restoration. *Transactions on Machine Learning Research*. [1](#), [2](#), [4](#)
- [10] P Kingma Diederik. Adam: A method for stochastic optimization. (*No Title*), 2014. [5](#)
- [11] Rizal Fathony, Anit Kumar Sahu, Devin Willmott, and J Zico Kolter. Multiplicative filter networks. In *International Conference on Learning Representations*, 2020. [2](#)
- [12] Ran Gal and Daniel Cohen-Or. Salient geometric features for partial shape matching and similarity. *ACM Transactions on Graphics (TOG)*, 25(1):130–150, 2006. [7](#)
- [13] Stephan J Garbin, Marek Kowalski, Matthew Johnson, Jamie Shotton, and Julien Valentin. Fastnerf: High-fidelity neural rendering at 200fps. In *Proceedings of the IEEE/CVF international conference on computer vision*, pages 14346–14355, 2021. [2](#)
- [14] Zongyu Guo, Gergely Flamich, Jiajun He, Zhibo Chen, and José Miguel Hernández-Lobato. Compression with bayesian implicit neural representations. *Advances in Neural Information Processing Systems*, 36:1938–1956, 2023. [2](#)
- [15] Jonathan Ho, Ajay Jain, and Pieter Abbeel. Denoising diffusion probabilistic models. *Advances in neural information processing systems*, 33:6840–6851, 2020. [2](#)
- [16] Mude Hui, Zihao Wei, Hongru Zhu, Fei Xia, and Yuyin Zhou. Microdiffusion: Implicit representation-guided diffusion for 3d reconstruction from limited 2d microscopy projections. In *Proceedings of the IEEE/CVF Conference on Computer Vision and Pattern Recognition*, pages 11460–11469, 2024. [2](#)
- [17] Muhammad Zubair Irshad, Sergey Zakharov, Katherine Liu, Vitor Guizilini, Thomas Kollar, Adrien Gaidon, Zolt Kira, and Rares Ambrus. Neo 360: Neural fields for sparse view synthesis of outdoor scenes. In *Proceedings of the IEEE/CVF International Conference on Computer Vision (ICCV)*, pages 9187–9198, 2023. [1](#)
- [18] Sijia Jiang, Jing Hua, and Zhizhong Han. Coordinate quantized neural implicit representations for multi-view reconstruction. In *Proceedings of the IEEE/CVF international conference on computer vision*, pages 18358–18369, 2023. [1](#)
- [19] Amirhossein Kazerouni, Reza Azad, Alireza Hosseini, Dorit Merhof, and Ulas Bagci. Incode: Implicit neural conditioning with prior knowledge embeddings. In *Proceedings of the IEEE/CVF Winter Conference on Applications of Computer Vision*, pages 1298–1307, 2024. [2](#)
- [20] Eastman Kodak. Kodak lossless true color image suite (photocd pcd0992), 1993. [6](#)
- [21] Zoe Landgraf, Alexander Sorkine Hornung, and Ricardo Silveira Cabral. Pins: progressive implicit networks for multi-scale neural representations. *arXiv preprint arXiv:2202.04713*, 2022. [2](#)
- [22] Ruoshi Liu, Rundi Wu, Basile Van Hoorick, Pavel Tokmakov, Sergey Zakharov, and Carl Vondrick. Zero-1-to-3: Zero-shot one image to 3d object. In *Proceedings of the IEEE/CVF international conference on computer vision*, pages 9298–9309, 2023. [2](#)
- [23] Zhen Liu, Hao Zhu, Qi Zhang, Jingde Fu, Weibing Deng, Zhan Ma, Yanwen Guo, and Xun Cao. Finer: Flexible spectral-bias tuning in implicit neural representation

- by variable-periodic activation functions. *arXiv preprint arXiv:2312.02434*, 2023. 1, 2
- [24] Ben Mildenhall, Pratul P Srinivasan, Matthew Tancik, Jonathan T Barron, Ravi Ramamoorthi, and Ren Ng. Nerf: Representing scenes as neural radiance fields for view synthesis. *Communications of the ACM*, 65(1):99–106, 2021. 1, 2
- [25] Adam Paszke, Sam Gross, Francisco Massa, Adam Lerer, James Bradbury, Gregory Chanan, Trevor Killeen, Zeming Lin, Natalia Gimelshein, Luca Antiga, et al. Pytorch: An imperative style, high-performance deep learning library. *Advances in neural information processing systems*, 32, 2019. 5
- [26] Songyou Peng, Michael Niemeyer, Lars Mescheder, Marc Pollefeys, and Andreas Geiger. Convolutional occupancy networks. In *Computer Vision–ECCV 2020: 16th European Conference, Glasgow, UK, August 23–28, 2020, Proceedings, Part III 16*, pages 523–540. Springer, 2020. 1
- [27] Guocheng Qian, Jinjie Mai, Abdullah Hamdi, Jian Ren, Aliaksandr Siarohin, Bing Li, Hsin-Ying Lee, Ivan Skokhodov, Peter Wonka, Sergey Tulyakov, et al. Magic123: One image to high-quality 3d object generation using both 2d and 3d diffusion priors. *arXiv preprint arXiv:2306.17843*, 2023. 2
- [28] Nithin Raghavan, Yan Xiao, Kai-En Lin, Tiancheng Sun, Sai Bi, Zexiang Xu, Tzu-Mao Li, and Ravi Ramamoorthi. Neural free-viewpoint relighting for glossy indirect illumination. In *Computer Graphics Forum*, page e14885. Wiley Online Library, 2023. 2
- [29] Nasim Rahaman, Aristide Baratin, Devansh Arpit, Felix Draxler, Min Lin, Fred Hamprecht, Yoshua Bengio, and Aaron Courville. On the spectral bias of neural networks. In *International conference on machine learning*, pages 5301–5310. PMLR, 2019. 2
- [30] Sameera Ramasinghe and Simon Lucey. Beyond periodicity: Towards a unifying framework for activations in coordinate-mlps. In *European Conference on Computer Vision*, pages 142–158. Springer, 2022. 2, 3, 5, 6, 7
- [31] Albert Reed, Thomas Blanford, Daniel C Brown, and Suren Jayasuriya. Implicit neural representations for deconvolving sas images. In *OCEANS 2021: San Diego–Porto*, pages 1–7. IEEE, 2021. 1
- [32] Christian Reiser, Songyou Peng, Yiyi Liao, and Andreas Geiger. Kilonerf: Speeding up neural radiance fields with thousands of tiny mlps. In *Proceedings of the IEEE International Conference on Computer Vision (ICCV)*, 2021. 2
- [33] Severi Rissanen, Markus Heinonen, and Arno Solin. Generative modelling with inverse heat dissipation. *arXiv preprint arXiv:2206.13397*, 2022. 2
- [34] Chitwan Saharia, Jonathan Ho, William Chan, Tim Salimans, David J Fleet, and Mohammad Norouzi. Image super-resolution via iterative refinement. *IEEE transactions on pattern analysis and machine intelligence*, 45(4):4713–4726, 2022. 1, 2
- [35] Vishwanath Saragadam, Jasper Tan, Guha Balakrishnan, Richard G Baraniuk, and Ashok Veeraraghavan. Miner: Multiscale implicit neural representation. In *European Conference on Computer Vision*, pages 318–333. Springer, 2022. 1, 2
- [36] Vishwanath Saragadam, Daniel LeJeune, Jasper Tan, Guha Balakrishnan, Ashok Veeraraghavan, and Richard G Baraniuk. Wire: Wavelet implicit neural representations. In *Proceedings of the IEEE/CVF Conference on Computer Vision and Pattern Recognition*, pages 18507–18516, 2023. 2, 3, 5, 6, 7
- [37] Siyuan Shen, Zi Wang, Ping Liu, Zhengqing Pan, Ruiqian Li, Tian Gao, Shiyong Li, and Jingyi Yu. Non-line-of-sight imaging via neural transient fields. *IEEE Transactions on Pattern Analysis and Machine Intelligence*, 43(7):2257–2268, 2021. 1
- [38] Rajhans Singh, Ankita Shukla, and Pavan Turaga. Polynomial implicit neural representations for large diverse datasets. In *Proceedings of the IEEE/CVF Conference on Computer Vision and Pattern Recognition*, pages 2041–2051, 2023. 2
- [39] Vincent Sitzmann, Julien Martel, Alexander Bergman, David Lindell, and Gordon Wetzstein. Implicit neural representations with periodic activation functions. *Advances in neural information processing systems*, 33:7462–7473, 2020. 1, 2, 3, 5, 6, 7, 8
- [40] Yang Song, Jascha Sohl-Dickstein, Diederik P Kingma, Abhishek Kumar, Stefano Ermon, and Ben Poole. Score-based generative modeling through stochastic differential equations. *arXiv preprint arXiv:2011.13456*, 2020. 4
- [41] Pratul P Srinivasan, Boyang Deng, Xiuming Zhang, Matthew Tancik, Ben Mildenhall, and Jonathan T Barron. Nerv: Neural reflectance and visibility fields for relighting and view synthesis. In *Proceedings of the IEEE/CVF Conference on Computer Vision and Pattern Recognition*, pages 7495–7504, 2021. 1
- [42] Yu Sun, Jiaming Liu, Mingyang Xie, Brendt Wohlberg, and Ulugbek S Kamilov. Coil: Coordinate-based internal learning for imaging inverse problems. *arXiv preprint arXiv:2102.05181*, 2021. 1
- [43] Matthew Tancik, Pratul Srinivasan, Ben Mildenhall, Sara Fridovich-Keil, Nithin Raghavan, Utkarsh Singhal, Ravi Ramamoorthi, Jonathan Barron, and Ren Ng. Fourier features let networks learn high frequency functions in low dimensional domains. *Advances in neural information processing systems*, 33:7537–7547, 2020. 2
- [44] Tianyu Wang, Xin Yang, Ke Xu, Shaozhe Chen, Qiang Zhang, and Rynson WH Lau. Spatial attentive single-image deraining with a high quality real rain dataset. In *Proceedings of the IEEE/CVF conference on computer vision and pattern recognition*, pages 12270–12279, 2019. 2
- [45] Zhou Wang, Alan C Bovik, Hamid R Sheikh, and Eero P Simoncelli. Image quality assessment: from error visibility to structural similarity. *IEEE transactions on image processing*, 13(4):600–612, 2004. 5
- [46] Shaowen Xie, Hao Zhu, Zhen Liu, Qi Zhang, You Zhou, Xun Cao, and Zhan Ma. Diner: Disorder-invariant implicit neural representation. In *Proceedings of the IEEE/CVF Conference on Computer Vision and Pattern Recognition (CVPR)*, pages 6143–6152, 2023. 2

- [47] Shaowen Xie, Hao Zhu, Zhen Liu, Qi Zhang, You Zhou, Xun Cao, and Zhan Ma. Diner: Disorder-invariant implicit neural representation. In *Proceedings of the IEEE/CVF Conference on Computer Vision and Pattern Recognition*, pages 6143–6152, 2023. [2](#)
- [48] Richard Zhang, Phillip Isola, Alexei A Efros, Eli Shechtman, and Oliver Wang. The unreasonable effectiveness of deep features as a perceptual metric. In *Proceedings of the IEEE conference on computer vision and pattern recognition*, pages 586–595, 2018. [5](#)
- [49] Ellen D Zhong, Tristan Bepler, Joseph H Davis, and Bonnie Berger. Reconstructing continuous distributions of 3d protein structure from cryo-em images. *arXiv preprint arXiv:1909.05215*, 2019. [1](#)

I-INR: Iterative Implicit Neural Representations

Supplementary Material

6. Additional Results

6.1. Additional Quantative Results

Table 7 presents a detailed comparison of our proposed method against the baseline across image fitting, denoising, and SR at $2\times$ for all three evaluation metrics (PSNR, SSIM, and LPIPS). Our iterative approach consistently enhances performance across tasks and different baselines, achieving superior reconstruction quality.

6.2. Additional Qualitative Comparison

We also present an additional qualitative comparison of our proposed method against SIREN, Gauss, and WIRE. Figures 9, 10, 11, 12, illustrates a comparative analysis for image fitting, SR at $2\times$ and $4\times$ scales, and image denoising, demonstrating the improvements achieved by our approach over baseline INRs. Our proposed method consistently outperforms single-shot baselines, demonstrating superior reconstruction quality across various models and tasks.

7. Additional Ablation Studies

Additional Reconstruction Steps Analysis: For SR at $2\times$, we further analyze the reconstruction quality of I-SIREN over multiple steps, comparing it to SIREN and the ground truth. As shown in Figure 13, the results demonstrate that with an increasing number of steps, details become more pronounced, and more high-frequency information is incorporated into the reconstruction.

Additionally, We analyze the impact of reconstruction steps on image fitting using the Kodak dataset (see Figure 14). Our findings indicate that the model achieves its highest PSNR at $steps = 4$, with the most significant gain occurring between $steps = 1$ and $steps = 2$. Beyond $steps = 2$, PSNR begins to plateau. Notably, even though PSNR decreases for $steps > 4$, perceptual quality continues to improve.

We also analyze the effect of reconstruction steps on image denoising performance using 40 images from the DIV2K dataset (see Figure 15). Our findings indicate that PSNR peaks at $steps = 2$ before gradually declining as $steps$ increases. Meanwhile, LPIPS improves until $step = 4$ and stabilizes around step 5. Beyond $steps = 4$, both PSNR and LPIPS degrade as I-INR begins reconstructing noise present in the data. At higher iterations, the model inadvertently reconstructs these distortions, leading to a decline in performance.

Feature Fusion: We conduct ablation studies on the final feature-fusion mechanism for signal reconstruction,

evaluating two strategies that combine the outputs of the *Backbone* and *Projection* modules (Figure 2a of main manuscript):

Multiplicative: $\mathcal{I}(x)_t = \text{Backbone} \odot \text{Projection}$,

Adaptive: $\mathcal{I}(x)_t = \text{Backbone} \times t + \text{Projection} \times (t - 1)$.

In *Multiplicative* fusion, the final output $\mathcal{I}(x)_t$ is obtained via element-wise multiplication of the Backbone and Projection outputs. The *Adaptive* method, conversely, uses the interpolation factor t to smoothly shift emphasis from the Backbone output (dominant at $t = 1$) toward the Projection output at higher values of t . Quantitative results comparing both fusion strategies for the image-fitting task are summarized in Table 8. Multiplicative fusion consistently outperforms Adaptive fusion, as evidenced by the results. Therefore, we adopt Multiplicative fusion as the standard approach for our method.

8. Training Setup

Table 9 presents the key hyperparameters for various experiments. These hyperparameters were chosen to maximize peak performance across different tasks.

Additionally, we used 2000 training iterations for image fitting, super-resolution (SR), and denoising tasks, while for object occupancy, we used 200 training iterations.

Table 7. Experimental results for Denoising, Image Fitting, and Super Resolution for **Baseline** model with **Ours**, evaluating their performance across three tasks. The best values in each column are highlighted in bold.

Task	Model	SIREN			Gauss			WIRE		
		PSNR \uparrow	SSIM \uparrow	LPIPS \downarrow	PSNR \uparrow	SSIM \uparrow	LPIPS \downarrow	PSNR \uparrow	SSIM \uparrow	LPIPS \downarrow
Image Fitting	Baseline	34.57	0.931	0.080	31.33	0.880	0.147	32.15	0.898	0.120
	Ours	37.53	0.961	0.032	31.93	0.884	0.124	33.73	0.924	0.077
Super Resolution	Baseline	26.77	0.763	0.414	25.19	0.709	0.538	26.14	0.749	0.457
	Ours	27.64	0.783	0.367	26.82	0.761	0.363	27.21	0.778	0.388
Denoising	Baseline	23.86	0.658	0.604	23.09	0.604	0.783	23.32	0.596	0.746
	Ours	25.59	0.619	0.540	24.20	0.612	0.533	24.76	0.645	0.490

Table 8. Comparison of fusion methods for the image-fitting task at $steps = 2$ on the Kodak dataset with Gaussian initial state ($\mathcal{Z} \sim \mathcal{N}(0, 1)$).

Fusion Method	I-SIREN			I-WIRE			I-Gauss		
	PSNR \uparrow	SSIM \uparrow	LPIPS \downarrow	PSNR \uparrow	SSIM \uparrow	LPIPS \downarrow	PSNR \uparrow	SSIM \uparrow	LPIPS \downarrow
Multiplicative	37.53	0.961	0.032	33.73	0.924	0.077	31.93	0.884	0.124
Adaptive	37.01	0.960	0.037	33.63	0.923	0.078	31.80	0.883	0.129

Table 9. Hyperparameter settings for I-INRs across different tasks.

Task	Parameter	I-Gauss	I-SIREN	I-WIRE
Image Fitting	ω	-	52	7
	σ	18	-	13
Image SR	ω	-	30	4
	σ	11	-	10
Image Denoising	ω	-	55	10
	σ	18	-	16
3D Occupancy	ω	-	55	10
	σ	17	-	20

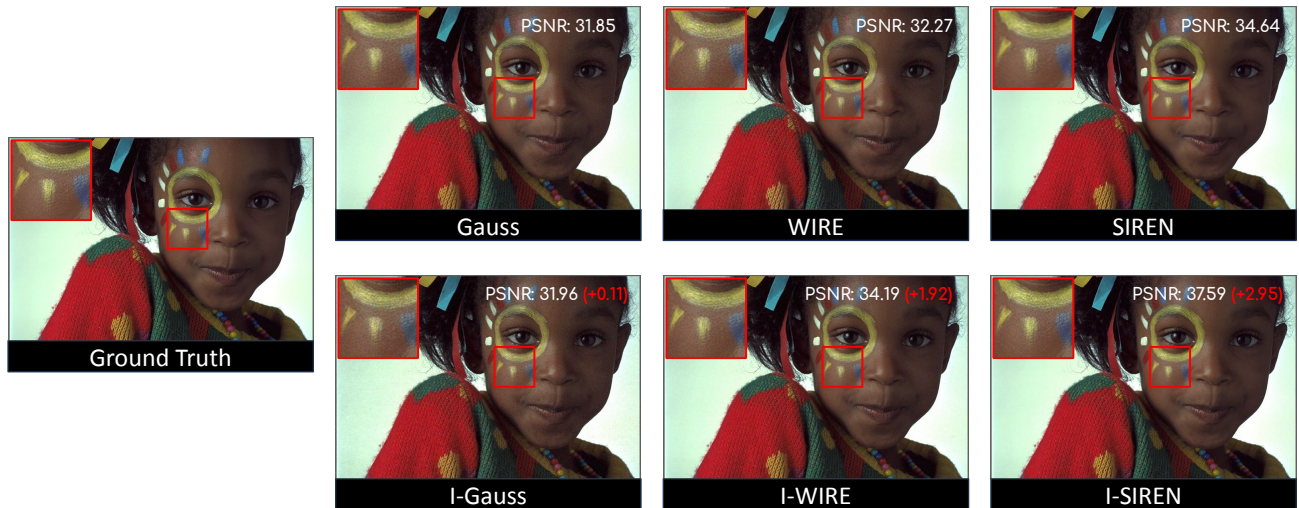


Figure 9. Image fitting results for different non-linearities and their iterative extensions (prefix "I").

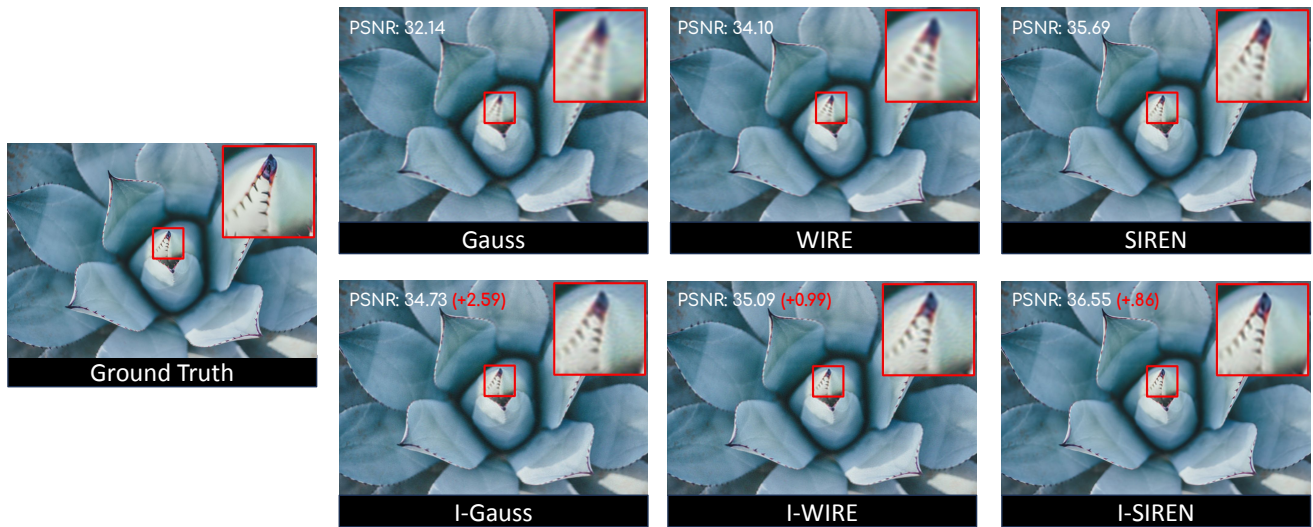


Figure 10. Visual quality comparison of super-resolution results at $2\times$ scale using various methods. The ground truth is compared against baseline INR methods SIREN, WIRE, Gauss, and their iterative counterparts. The iterative approaches consistently achieve sharper reconstructions with fewer artifacts, effectively preserving finer details and high-frequency structures.

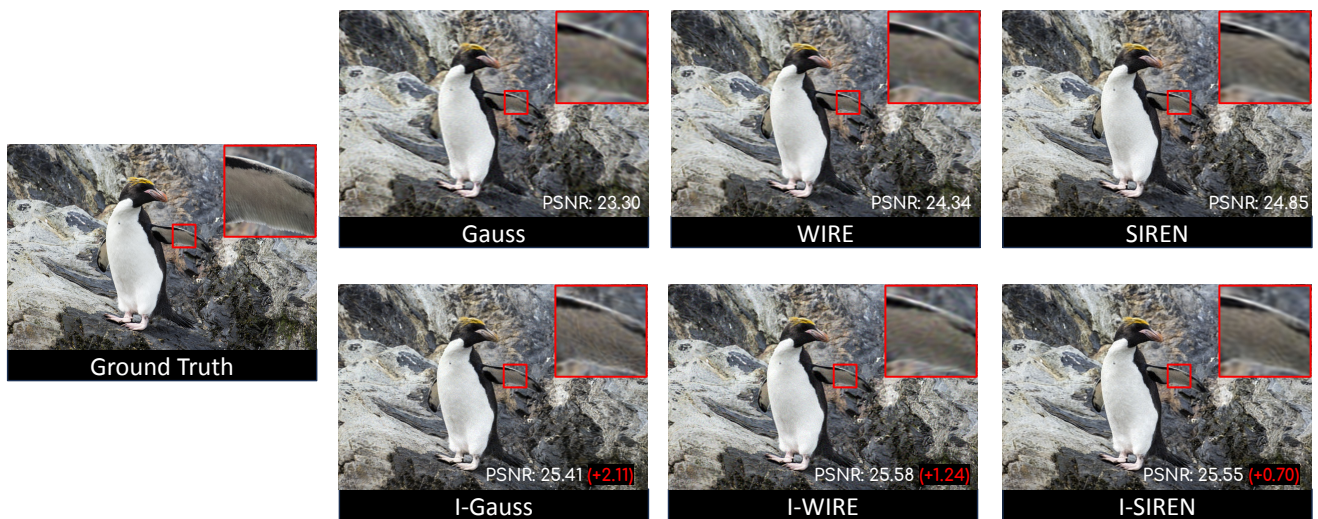


Figure 11. Visual quality comparison of super-resolution results at $4\times$ scale using various methods. The ground truth is compared against baseline INR methods SIREN, WIRE, Gauss, and their iterative counterparts. The iterative approaches consistently achieve sharper reconstructions with fewer artifacts, effectively preserving finer details and high-frequency structures.



Figure 12. Visual comparison of denoising results using various methods. The ground truth is compared against noisy input, baseline methods SIREN, WIRE, and Gauss, as well as their iterative counterparts. I-INR demonstrates superior artifact reduction and detail preservation compared to their non-iterative counterparts.

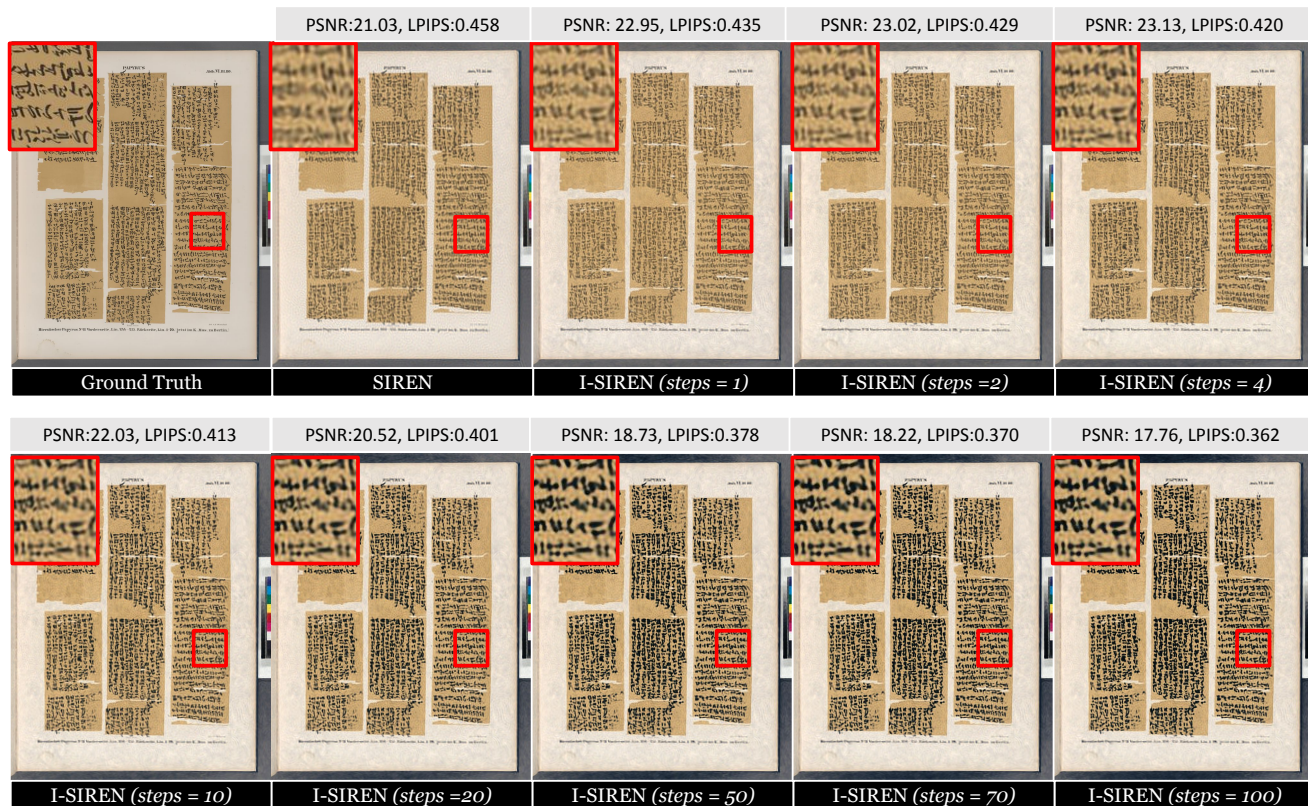


Figure 13. Analysis of I-SIREN's performance for super-resolution at $2\times$ resolution across different steps. I-SIREN achieves peak PSNR at $steps = 4$, where further increasing steps enhances perceptual quality.

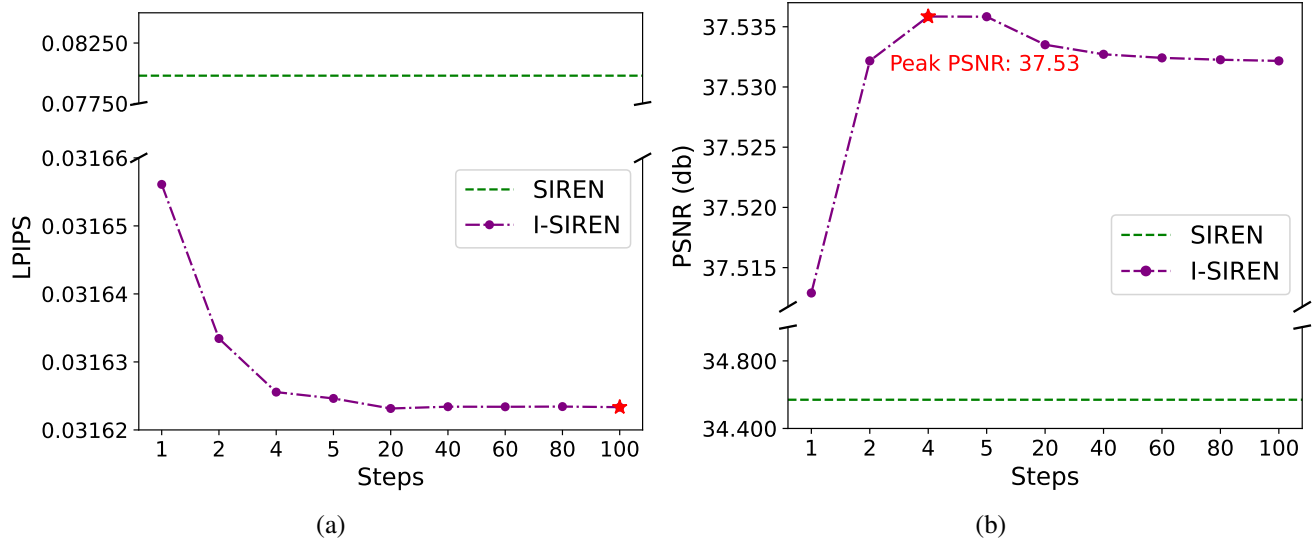


Figure 14. Analysis of I-SIREN's performance for image fitting across different iteration steps. (a) Increasing the number of steps consistently improves perceptual quality. (b) PSNR reaches its highest performance at $steps = 4$, and while additional iterations slightly reduce PSNR, it remains superior to the baseline.

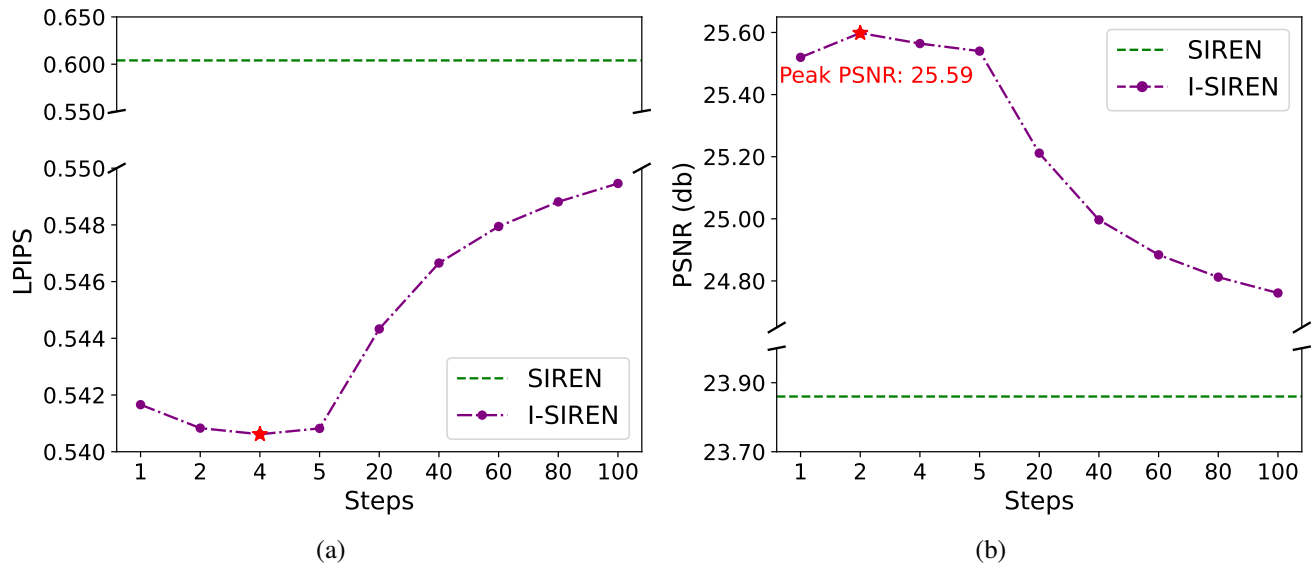


Figure 15. Analysis of I-SIREN's performance for denoising across different reconstruction steps. (a) LPIPS improves until step 4 and stabilizes around step 5. (b) PSNR reaches its peak at $steps = 2$, but further iterations degrade performance.